Short Article

Developmental Cell

Inhomogeneous mechanotransduction defines the spatial pattern of apoptosis-induced compensatory proliferation

Graphical abstract

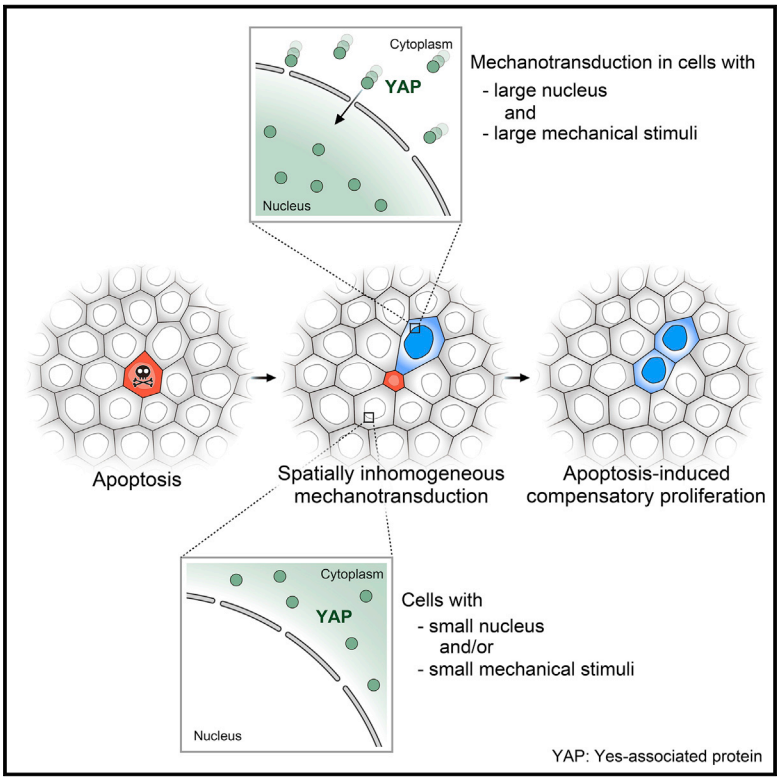

Highlights

- Only a restricted number of neighboring cells are selected to divide upon apoptosis
- Pattern of division is defined by inhomogeneous YAP-mediated mechanotransduction
- Inhomogeneity arises from non-uniform force and nuclear size in neighboring cells

Authors

Takumi Kawaue, Ivan Yow, Yuping Pan, ..., Tetsuya Hiraiwa, Benoit Ladoux, Yusuke Toyama

Correspondence

dbsty@nus.edu.sg

In brief

Only a restricted number of neighboring cells are selected to divide and compensate for cell loss upon apoptosis. Kawaue et al. show that spatial inhomogeneity in mechanotransduction accounts for this uneven compensatory proliferation. Such inhomogeneity arises from the non-uniform nuclear size and mechanical force applied to the neighboring cells during apoptosis.

Kawaue et al., 2023, Developmental Cell *58*, 267–277
February 27, 2023
https://doi.org/10.1016/j.devcel.2023.01.005

CellPress

Developmental Cell

CellPress

Short Article

Inhomogeneous mechanotransduction defines the spatial pattern of apoptosis-induced compensatory proliferation

Takumi Kawaue,[1,2,6] Ivan Yow,[1,6] Yuping Pan,[1,6] Anh Phuong Le,[1] Yuting Lou,[1] Mavis Loberas,[1] Murat Shagirov,[1] Xiang Teng,[1] Jacques Prost,[3] Tetsuya Hiraiwa,[1] Benoit Ladoux,[4] and Yusuke Toyama[1,5,7,*]

[1]Mechanobiology Institute, National University of Singapore, Singapore
[2]Institute for Integrated Cell-Material Sciences, Kyoto University, Kyoto, Japan
[3]Physico Chimie Curie, Institut Curie, CNRS, UMR 168, 75005 Paris, France
[4]Université Paris Cité, CNRS, Institut Jacques Monod, F-75013 Paris, France
[5]Department of Biological Sciences, National University of Singapore, Singapore
[6]These authors contributed equally
[7]Lead contact
*Correspondence: dbsty@nus.edu.sg
https://doi.org/10.1016/j.devcel.2023.01.005

SUMMARY

The number of cells in tissues is controlled by cell division and cell death, and its misregulation could lead to pathological conditions such as cancer. To maintain the cell numbers, a cell-elimination process called apoptosis also stimulates the proliferation of neighboring cells. This mechanism, apoptosis-induced compensatory proliferation, was originally described more than 40 years ago. Although only a limited number of the neighboring cells need to divide to compensate for the apoptotic cell loss, the mechanisms that select cells to divide have remained elusive. Here, we found that spatial inhomogeneity in Yes-associated protein (YAP)-mediated mechanotransduction in neighboring tissues determines the inhomogeneity of compensatory proliferation in Madin-Darby canine kidney (MDCK) cells. Such inhomogeneity arises from the non-uniform distribution of nuclear size and the non-uniform pattern of mechanical force applied to neighboring cells. Our findings from a mechanical perspective provide additional insight into how tissues precisely maintain homeostasis.

INTRODUCTION

Apoptosis, or programmed cell death, is a mechanism by which unnecessary, aged, or damaged cells are eliminated.[1] To maintain the homeostatic cell number in epithelium and organs, an apoptotic event can also induce proliferation of neighboring cells, a process termed apoptosis-induced compensatory proliferation, takes place. This phenomenon of compensatory proliferation was originally described more than 40 years ago.[2] Haynie and Bryant investigated how *Drosophila* imaginal wing disc responds to damage induced by X-ray irradiation. Although the irradiation of *Drosophila* larvae killed ~60% of the cells in the wing disc, the remaining cells were able to recover and develop as adult wings with normal structure and size. This suggested that there are cellular mechanisms that promote cell division upon tissue damage to compensate for the cell loss. Since then, the mechanisms of compensatory proliferation, especially the role of mitogenic signals secreted by the apoptotic cell, have been investigated.[3,4] For instance, in *Drosophila*, it is well characterized that the secretion of Decapentaplegic (Dpp) and Wnt/Wingless (Wg) mitogens from the apoptotic cell results in cell proliferation in neighboring cells.[5–9] In mice[10] and a mammalian cell line,[11] the pro-inflammatory metabolite, Prostaglandin E2 (PGE2), is produced and secreted by the apoptotic cell and stimulates cell growth. Notably, it is sufficient for a limited number of the neighboring cells to divide to compensate for the cell loss due to apoptosis. This raises a possibility that biochemical signals secreted by the apoptotic cell, which could influence all the neighboring cells, are crucial but may not be solely responsible to explain this spatial inhomogeneity of compensatory proliferation. More recently, the apoptotic process, especially in the context of cell extrusion, has been associated with mechanical force. An apoptotic cell is expelled from a tissue through the contraction of an actomyosin cable formed in the dying cell as well as in the neighboring cells or via lamellipodium crawling by adjacent cells.[12–16] This cell extrusion process further alters the surrounding tissue tension and morphogenesis.[17–20] Here, we considered the mechanical force associated with an apoptotic process and elucidate how only a small number of cells around an apoptotic cell undergo cell division. We found that the spatial inhomogeneity in mechanotransduction through the growth-promoting transcriptional co-activator Yes-associated protein (YAP) in the neighboring tissue is responsible for the inhomogeneity of compensatory proliferation. Such

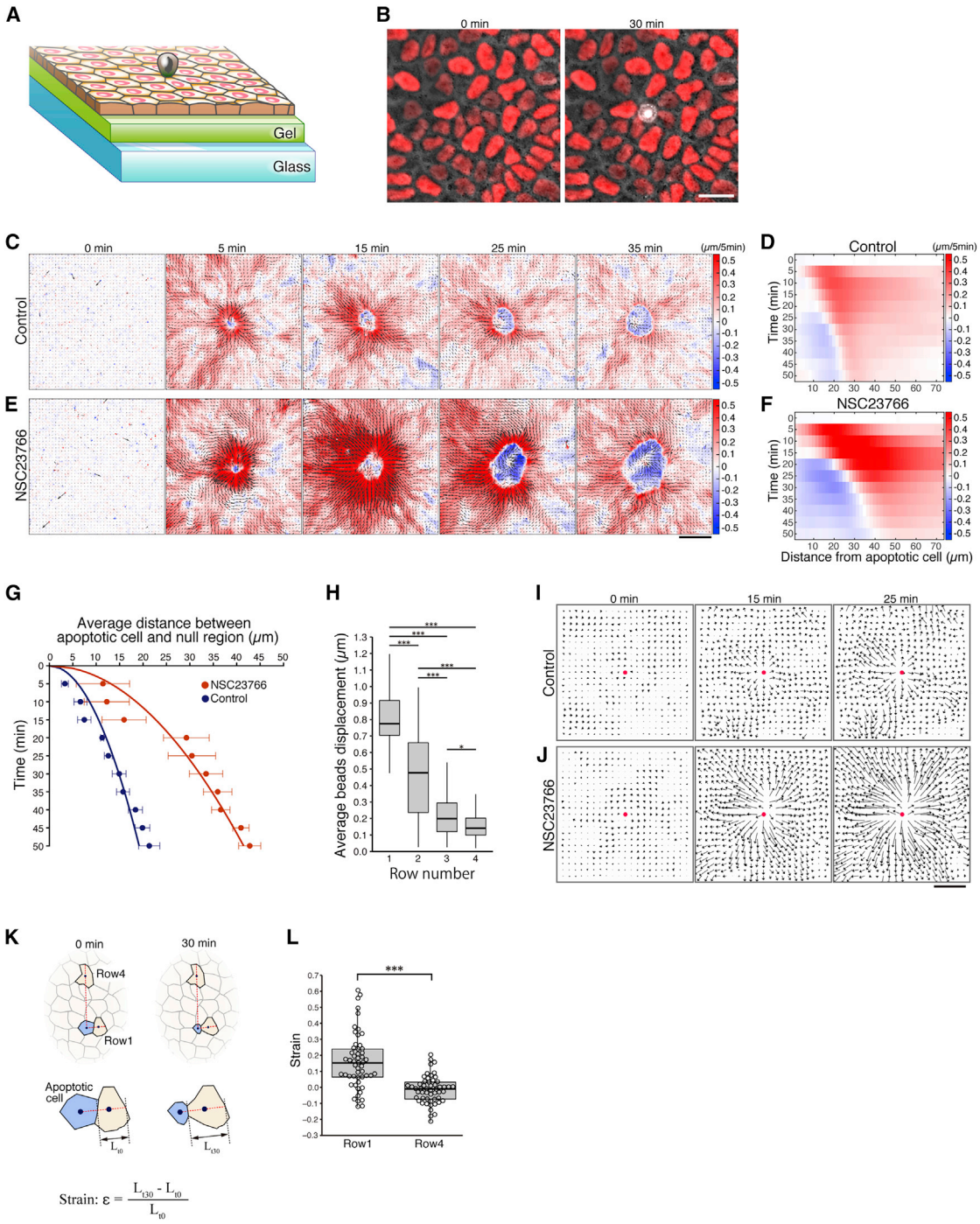

Figure 1. Mechanical force propagation and stretching in the neighboring tissue upon apoptosis

(A) Schematic of the experimental setup. A confluent MDCK monolayer (orange) is cultured on a polydimethylsiloxane (PDMS) gel (green). An apoptotic cell is highlighted in gray.

(B) Time-lapse images of an apoptotic cell extrusion within an MDCK monolayer.

(C and E) Heatmaps with vectors showing the direction and magnitude of bead radial velocity in control and NSC23766-treated tissues. The color bar indicates the magnitude of the outward (red) and inward (blue) velocity from the apoptotic cell in μm/5 min.

(D and F) Kymographs of the average radial velocity in (C) and (E).

(G) Average distance from the apoptotic cell to the static region, the white region between red (outward) and blue (inward), in (D) and (F). Time 0 represents the onset of cell extrusion. Data are mean ± SEM. n = 5 ROIs for both control and NSC23766.

(H) Average bead displacement at different distances from the apoptotic cell (row number) at 1 min after apoptosis. Data are mean ± SD; *p < 0.05 and ***p < 0.001, one-way ANOVA and Levene test followed by a Tukey-Kramer test. n = 7 ROIs in 3 independent experiments.

(legend continued on next page)

inhomogeneous mechanotransduction results from the combination of the non-uniform distribution of nuclear size, which is inherent in tissues, and the non-uniform pattern of mechanical force applied to the neighboring cells upon apoptosis.

RESULTS

Mechanical force propagation and stretching in the neighboring tissue upon apoptosis

To understand how an apoptotic event mechanically influences neighboring cells, we established an *in vitro* platform to quantitatively measure the changes in mechanical force among neighboring tissue upon cell death in Madin-Darby canine kidney (MDCK) epithelial cells (Figure 1A). DNA damage and subsequent apoptotic cell extrusion (Figure 1B) in the desired cell were induced by using a UV laser[14,21] among a tissue that was cultured on deformable substrates made from elastic polydimethylsiloxane (PDMS) gel with fluorescent beads.[22] Upon the induction of apoptosis, a wave-like propagation of bead displacement, which is the proxy for substrate deformation, was observed (Video S1). Particle image velocimetry (PIV) analysis of the movement of the fluorescent beads (Figure 1C) showed that, initially, the beads moved away from the apoptotic cell (red, t = 5 min in Figure 1C) and that this displacement was largest at the nearest neighboring cells (Figure 1H, STAR Methods). In addition to the outward movement, the inward movement of the substrate emerged at the region close to the extrusion site (blue, Figure 1C). To quantitatively understand the substrate deformation, we plotted the kymograph of the average radial velocity of the beads as a function of distance from the apoptotic cell (Figure 1D, STAR Methods). In between the outwardly and inwardly moving substrate, there was a small region of substrate that showed transiently static behavior (i.e., no or balanced inward and outward movement), and this transiently static region shifted away from the extrusion site over time (white in Figure 1D). We adopted this static region as one of the hallmarks of substrate deformation and found that the wave propagated a distance of 21.3 ± 2.3 μm (mean ± SEM) away from the dead cells in an hour (Figure 1G). Comparable wave-like propagation was observed upon spontaneous apoptotic cell extrusion without using UV laser induction (Figure 3A, hereafter referred to as spontaneous extrusion). To understand the cause of the substrate deformation, we treated the tissue with the Rac1 inhibitor NSC23766 to inhibit lamellipodial cell crawling. Lamellipodia crawling is known to occur in neighboring cells and contributes to apoptotic cell extrusion[14,16] and to deform the substrate to the direction opposite to the cell migration. Although we predicted that NSC23755 treatment would diminish substrate deformation upon apoptosis, we found that the wave propagation increased to a distance of 42.8 ± 2.4 μm in an hour (Figures 1E–1G; Video S1). We then tracked the tissue dynamics by differential interference contrast (DIC) imaging and found that the cells moved away from the dead cell in both control and NSC23766-treated tissue (Figures 1I and 1J; Video S2). We reasoned that the release of epithelial tissue pre-tension, which is an inherent tissue characteristic generated by actomyosin-mediated contractility, leads to the relaxation and the outward movement of the tissue around the apoptotic cell. Indeed, we previously reported a reduction of the adherens junction molecule E-cadherin between apoptotic and neighboring cells after caspase-3 activation in the apoptotic cell in *Drosophila* epithelia[13] and MDCK cells.[23] This reduction of E-cadherin leads to disengagement of the cell-cell junction between apoptotic and neighboring cells and a release of the tissue pre-tension.[13] To further validate our reasoning, we compared the tissue pre-tension between control and NSC23766-treated monolayer by laser ablation at the cell-cell junction[24] without induction of apoptosis. The junctional tension in the NSC23766-treated tissue is higher than that of the control tissue (Figures S1A–S1C), which is consistent with the larger wave propagation in NSC23766-treated tissue. We further found that the relative position between the focal adhesions of the neighboring cells and the beads embedded in the substrate did not change drastically during wave propagation, indicating that there is minimal sliding between tissue and the substrate during wave propagation (Figure S1D). Together, our data reveal that the tissue moves away from the dead cell due to the relaxation of the tissue pre-tension upon apoptosis. The wave-like dynamics of the substrate gel caused by the release of the pre-tension of tissue upon apoptosis can be explained by a physical model based on a linear elasticity theory.[25]

A kymograph of the radial average velocity of the beads showed that there was an inward movement of the substrate toward the apoptotic cell (blue in Figures 1C–1F). We speculate that this is, in part, due to the formation and the contraction of the actomyosin cable in the neighboring cells.[12,16,23] The appearance of the inward movement emerged around 5–10 min after the initial outward movement, consistent with the timing of formation and initiation of actomyosin cable contraction. These observations imply that the neighboring cells are stretched by apoptotic cell extrusion. Indeed, measuring the strain of the neighboring cells showed that the nearest neighbor cells underwent 16.2 ± 2.3% stretch, which is significantly larger than cells further away from the dead cell (Figures 1K and 1L). Taken together, we conclude that the cells in the vicinity of the apoptotic cell experience tensile stretching, which is due to the combination of tissue relaxation and apoptosis-associated actomyosin cable contraction.

A small number of neighboring cells show nuclear translocation of YAP and cell-cycle progression upon apoptosis

To address whether this stretching of the neighboring tissue would further influence the biochemical signaling within the surrounding cells, we examined the dynamics of Yes-associated protein (YAP), a growth-promoting transcription co-activator

(I and J) Velocity vectors of tissue movement upon apoptosis in control and NSC23766-treated conditions. Red dots, apoptotic cells.
(K) Diagram illustrating cellular strain (ε) for cells near and far (row 1 and row 4) from an apoptotic cell (blue). L_{t0} and L_{t30} represent the length of the cells at 0 and 30 min after apoptosis.
(L) Strain of cells in row 1 and row 4 at 30 min after apoptosis. Data are mean ± SD; ***p < 0.001, Mann-Whitney U test. n = 53 cells for both row 1 and row 4 from 7 ROIs in 3 independent experiments. Scale bars: 20 μm in (B) and 50 μm in (C), (E), (I), and (J).

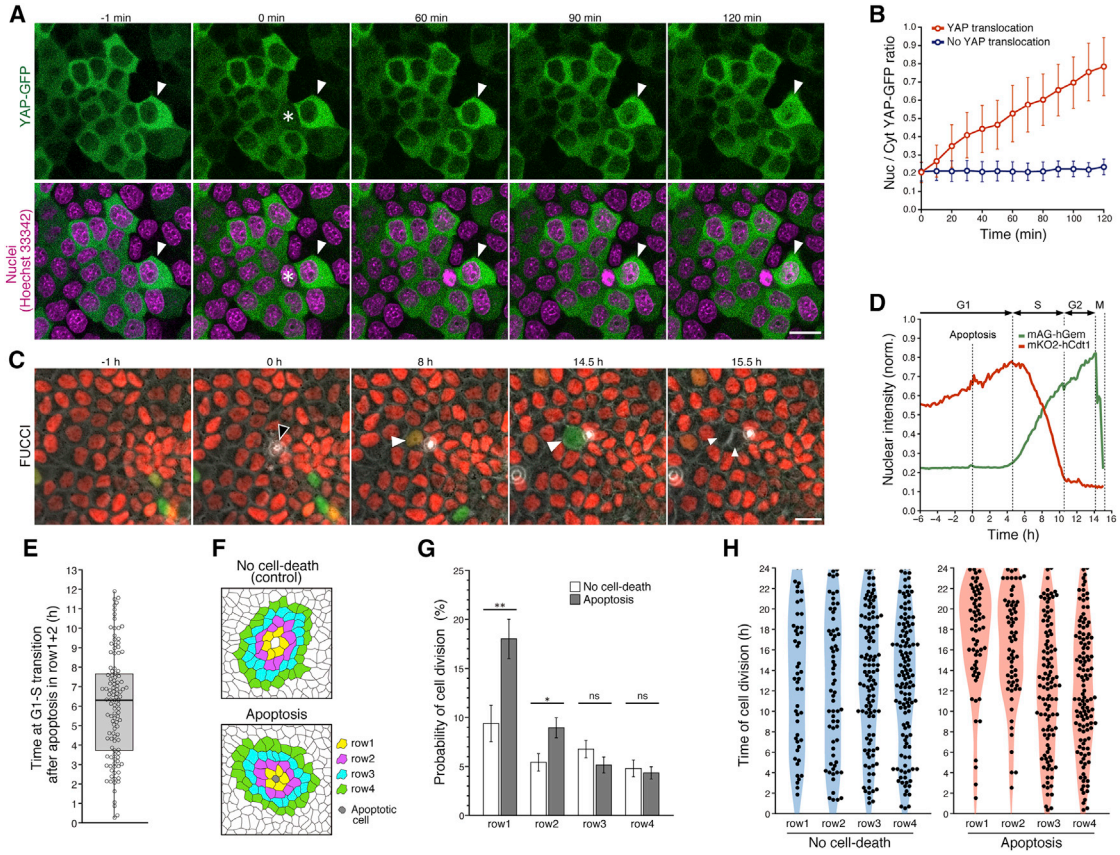

Figure 2. A small number of neighboring cells show nuclear translocation of YAP and cell-cycle progression upon apoptosis

(A) Time-lapse images showing YAP nuclear translocation (white arrowhead) within an MDCK YAP-GFP monolayer. Time 0 represents the onset of laser-induced apoptosis (asterisk).

(B) Evolution of the nuclear/cytoplasmic (Nuc/Cyt) YAP-GFP ratio in cells surrounding an apoptotic cell. Cells were classified as having YAP translocation ($I_{nuc/cyt} \geq 0.5$, red) or no translocation ($I_{nuc/cyt} < 0.5$, blue) based on their Nuc/Cyt ratio at 2 h after apoptosis. n = 25 ($I_{nuc/cyt} \geq 0.5$) and 17 ($I_{nuc/cyt} < 0.5$) cells in 10 ROIs from 6 independent experiments. Data are mean ± SD.

(C) Time-lapse images showing the cell-cycle progression of a cell (white arrowhead) next to spontaneous apoptosis (black arrowhead) within an MDCK FUCCI monolayer.

(D) Representative normalized fluorescence intensities of mKO2-Cdt1 (red) and mAG-hGem (green) in a cell shown in (C) (white arrowhead). The dotted lines indicate the time points of the cell-cycle phase transition.

(E) Distribution of the time of G1-S phase transition in cells surrounding the apoptotic cell. Data are mean ± SD. n = 114 cells from 54 ROIs in 6 independent experiments.

(F) Illustration of cells in each cell row (rows 1–4) surrounding a live or apoptotic cell.

(G) Probability of cell division for each row of cells within 24 h after extrusion. Cells that underwent the G1-S phase transition prior to extrusion or arbitrarily defined time 0 were excluded from the analysis for apoptosis or no cell death case, respectively. Data are mean ± SD; not significant (ns), *$p < 0.05$ and **$p < 0.01$, Mann-Whitney U test.

(H) Distribution of the time of cell division at each row of cells around control (no cell death) and apoptotic cells. Time 0 represents the time of spontaneous apoptosis. Data shown in (G) and (H) are from n = 54 ROIs in 6 independent experiments for both control and apoptosis. Scale bars: 20 μm in (A) and (C).

See also Figure S2.

and an effector of the Hippo pathway.[26] YAP is also known as a mechanotransducer that transforms the physical stimuli that cells experience through mechanosensing into intracellular biochemical signals.[27] Upon mechanical stimuli, YAP translocates into the nucleus, which further promotes downstream transcriptional programs including cell proliferation.[28] We imaged the localization of YAP in the neighboring cells of an apoptotic cell by using MDCK cells that stably express YAP-GFP, which shows similar distribution as endogenous YAP (STAR Methods, Figure S2A). Only a fraction of neighboring cells exhibited nuclear translocation of YAP (Figures 2A and 2B; Video S3) as cells undergo stretching (Figure S2B). Furthermore, the cells close to the apoptotic cell had a higher probability of YAP nuclear translocation, compared with cells further away from the dying cell (Figure S2C). Similar YAP nuclear translocation was observed in response to spontaneous extrusion and was associated with cell division (Figures S2D and S2E). To further understand the consequence of apoptosis-associated YAP nuclear translocation, we imaged the cell-cycle progression of the neighboring cells around spontaneous extrusion by using

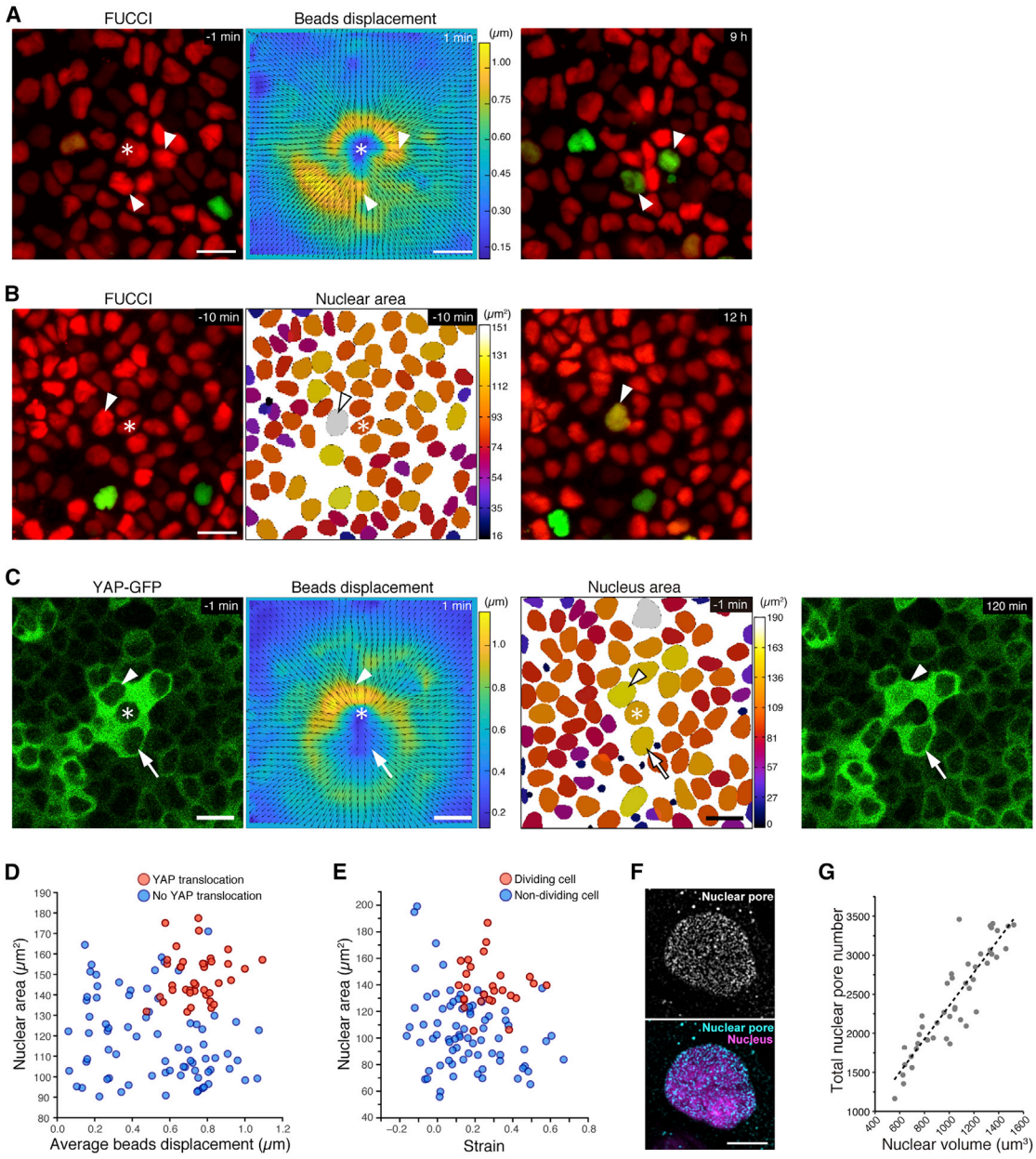

Figure 3. Inhomogeneous cell division arises from the combination of spatial inhomogeneities in force propagation and nuclear size

(A and B) Time-lapse images showing an MDCK FUCCI monolayer before (left) and after (right) spontaneous apoptosis (asterisk), a heatmap with vectors of bead displacement at 1 min after extrusion (center in A), and a heatmap of the nuclear area at 10 min before extrusion (center in B). A small number of neighboring cells (white arrowhead) show cell-cycle progression.

(C) Time-lapse images of MDCK YAP-GFP monolayer before (left) and after (right) laser-induced apoptosis (asterisk), and a heatmap of bead displacement and nuclear area (middle). A cell associated with a large nucleus and large bead displacement shows YAP nuclear translocation (white arrowhead), but a cell associated with a large nucleus and small displacement does not (white arrow).

(D) A scatter plot showing how cells with (red) or without (blue) YAP nuclear translocation correlate with the nuclear area and average bead displacement. Nuclear area and bead displacement were measured at 1 min before and after apoptosis. YAP translocation was measured 2 h after apoptosis. n = 115 cells in 36 ROIs from 9 independent experiments.

(E) A scatter plot showing how dividing (red) and non-dividing (blue) MDCK FUCCI cells correlate with the nuclear area and the strain experienced by the cells. The strain was measured at 30 min after spontaneous apoptosis. n = 103 cells in 16 ROIs from 6 independent experiments.

(F) Immunostaining for nuclear pore complex of a WT MDCK cell.

(G) Graph showing the total number of nuclear pore complexes as a function of nuclear volume. n = 45 cells in 2 independent experiments. Scale bars: 20 μm in (A)–(C) and 10 μm in (F).

See also Figure S3.

MDCK cells with the cell-cycle reporter fluorescent ubiquitination-based cell-cycle indicator, FUCCI.[29] The cells were first serum-starved for 24 h to synchronize the cell cycle at G1 phase. Prior to imaging, serum-free media was replaced with fresh media containing serum. We found that only a few neighboring cells underwent cell-cycle progression from G1 to S phase at around 6–7 h after apoptosis (Figures 2C–2E; Video S4). The cells close to the apoptotic cell (rows 1 and 2) had a higher probability of mitosis (Figures 2F and 2G). Moreover, the probability (Figure S2F) and the number (Figure 2H) of mitosis increased at around 16–24 h after apoptosis. Such characteristics are distinct from the cells irrelevant to and more than 2 cells away from apoptosis (Figures 2G, 2H, and S2F). Similar cell-cycle progression was observed in response to UV-induced apoptosis (Figure S2G). Together, our data consistently showed that only a few neighboring cells undergo cell division associated with YAP nuclear translocation upon apoptosis (Figures 2 and S2).

Spatial inhomogeneities in force propagation and nuclear size define which of the neighboring cells undergo cell division following apoptosis

To uncover what defines this spatial inhomogeneity of cell division, we sought out factors that are not homogeneous in space. First, the substrate deformation as measured by bead displacement is spatially inhomogeneous (Figures 1C and 3A). We noticed that cells that underwent cell-cycle progression upon apoptosis spatially correlated to the region with large displacement (Figure 3A), indicating cells that experienced a larger displacement and consequently underwent more stretching have a higher chance to undergo cell division. Second, the spatial distribution of the size of the nucleus is spatially inhomogeneous. We found that the cells that underwent cell-cycle progression upon apoptosis tended to have a larger nucleus before the onset of apoptosis (Figure 3B). To address whether these two spatially inhomogeneous factors, i.e., substrate deformation and nucleus size, are both required for cell proliferation, we simultaneously monitored bead displacement, nucleus size, and YAP localization. We found a case of 2 neighboring cells that both had a large nucleus (arrowhead and arrow, Figure 3C); however, only the cell located in the region that underwent large bead displacement showed YAP nuclear translocation (arrowhead, Figure 3C). To further solidify our observation, we analyzed more than 100 cells that were in the vicinity of UV-induced apoptotic cells (Figure 3D). Only cells with a large nucleus that experienced large bead displacement showed clear YAP nuclear translocation (red in Figures 3D and S3A). By contrast, cells with a large nucleus that experienced small bead displacement or any cells with a small nucleus did not show clear YAP nuclear translocation (blue in Figure 3D). In addition, by analyzing the relationship between strain (Figure 1K), nucleus size, and cell-cycle progression measured by FUCCI, we found that only the cells around spontaneous extrusion with a large nucleus that experienced large strain underwent cell division (red in Figures 3E and S3B). To rationalize how strain and nuclear size regulate YAP nuclear translocation and cell proliferation, we measured the number of nuclear pore complexes depending on nuclear size (Figures 3F and 3G). The nuclear pore complex is a known structure that facilitates YAP transport from the cytoplasm to the nucleus in a tension-dependent manner.[30] We found that the number of nuclear pores increases with the size of the nucleus (Figures 3G and S3C) and speculated that the larger nuclear size helps nuclear translocation of YAP upon mechanical stretching. Together, we found that the spatially limited cell division around the apoptotic process is defined by the spatial inhomogeneity of pre-tension release (measured by bead displacement) that leads to the strain of a cell and the spatial inhomogeneity of nuclear size.

To understand to what extent the difference in nuclear size before the onset of apoptosis (Figures 3D and 3E) represented the intrinsic inhomogeneity of nuclear size among tissue, we measured the changes in nuclear size during cell-cycle progression. The nucleus size typically increased by ~10% during the progression from G1 to G2 phase (Figure S3D). Moreover, we observed a wide distribution in nuclear size within a tissue with a full width at half maximum (FWHM), which represents the spread of the distribution, of 50.4 μm^2 (Figure S3E). We thus conclude that the difference in nuclear size between cells that divided or not (Figures 3E and S3B) and between cells that showed YAP nuclear translocation or not (Figures 3D and S3A) did not predominantly arise from the changes in the nuclear size during cell division but from the intrinsic inhomogeneity of nuclear size among tissue.

Compensatory proliferation requires force propagation through the substrate

To understand to what extent the mechanical factors shown earlier play causal roles in compensatory proliferation in addition to mitogenic signaling from the apoptotic cell, which is known to contribute to compensatory proliferation,[3,4] we aimed to modulate force propagation without altering the biochemical interaction between apoptotic and neighboring cells. To this end, we did not change the mechanical properties of the PDMS substrate but altered the size of the tissue or the friction between the gel substrate and the glass-bottom Petri dish. We speculated that tissue pre-tension decreases as tissue size reduces[31] and first altered the size of the tissue by using microcontact printing technology (STAR Methods). The size of the mini-tissue was reduced until the bead displacement diminished. A mini-tissue of 100 μm diameter (Figure 4A) showed a reduced bead displacement (Figures 4B and 4C; Video S5), consistent with the reduction of junctional tension in the mini-tissue (Figures S1A–S1C). Under this condition, the neighboring cells failed to translocate YAP into the nucleus (Figures 4D and 4E; Video S5) regardless of nucleus size (Figure 4F) upon the induction of apoptosis in a cell in the middle of a mini-tissue. Our theoretical model based on linear elasticity theory[25] predicted that the gel substrate with 50 μm thickness is weakly adhered to the surface of the glass-bottom Petri dish (Figure 1A) and that increasing this adhesion would suppress the wave propagation. To test this prediction, the dish was silanized with 3-aminopropyl trimethoxysilane (APTES) to increase the adhesion of the gel to the glass (STAR Methods, Figure 4G). We found that under this condition the bead displacement upon apoptosis was diminished (Figures 4H and 4I) and YAP nuclear translocation in the neighboring cells was abolished regardless of nuclear size (Figures 4J–4L). In addition, cell-cycle progression in neighboring cells surrounding a spontaneous extrusion was also abolished with APTES treatment (Figures 4M and 4N). Taken together, our data further support the idea that modulation of the mechanical status of the neighboring

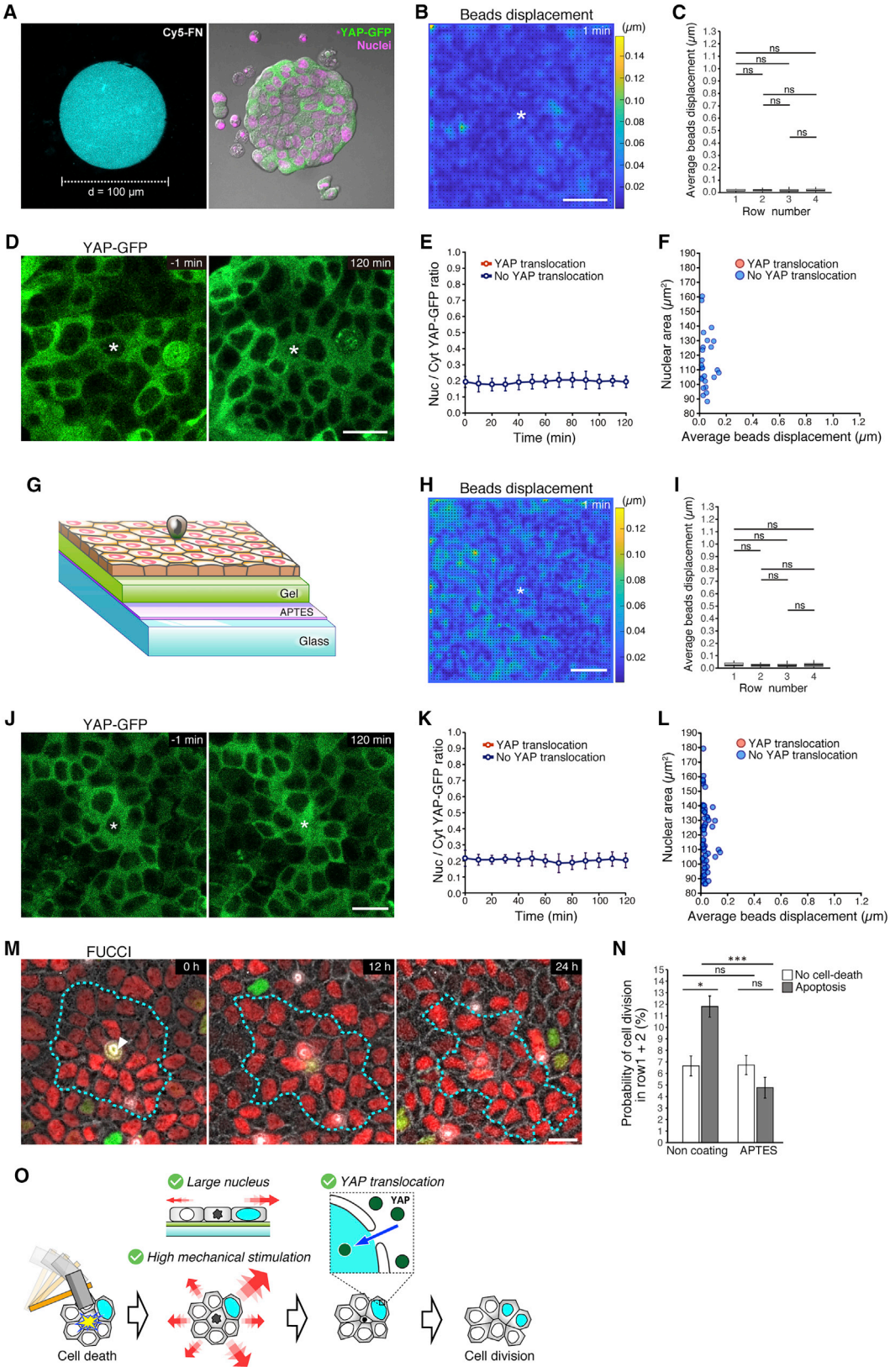

(legend on next page)

cells of the apoptotic cell through the substrate is required for the nuclear translocation of YAP, cell-cycle progression, and cytokinesis of the neighboring cells.

DISCUSSION

In this study, we addressed a long-standing question of how only a small number of cells around an apoptotic cell undergo cell division to sustain homeostasis of the cell number in a tissue (Figure 4O). The spatial inhomogeneity of cell division in response to the apoptotic process is associated with inhomogeneous mechanotransduction, characterized by the nuclear translocation of YAP, and arises from the combination of the large strain and the large nuclear size of the neighboring cells, which is inherent in tissues. The suppression of mechanical stimulus without altering the cell-cell contact between apoptotic and neighboring cells resulted in a lack of mechanotransduction and cell division (Figures 4A–4N). These results highlighted that force propagation through the deformable substrate, which has been overlooked, plays a causal role in compensatory proliferation. Our theoretical model[25] suggested that the experimental condition where the gel substrate is weakly adhered to a glass-bottom dish (Figure 1A) has mechanical features analogous to layers of tissue with viscoelasticity. We speculate that stratified epithelium, such as skin,[32] shares similar mechanotransduction mechanisms in compensatory proliferation. By contrast, compensatory proliferation may not be apparent with a substrate where apoptosis-associated force cannot be propagated, such as a glass substrate or the gel substrate that strongly adhered to a glass-bottom dish (Figure 4G), which behaves as an elastic substrate and has been used for traction force microscopy.

One obvious question is whether the number of nuclear pore complexes is the only factor correlated with nuclear size and YAP nuclear translocation. Interestingly, it has been shown that large nuclei are much softer than small nuclei.[33] It is possible that large nuclei are more deformable, and therefore, an increase in nuclear membrane curvature upon cell stretching promotes YAP nuclear translocation through the nuclear pore complex.[30] Another key question is how biochemical signaling that emerges from the apoptotic process contributes to compensatory proliferation. Our data support the idea that mitogenic signals secreted without specific direction from the apoptotic cell are crucial as demonstrated before,[5–11] but not solely sufficient, to explain the spatially inhomogeneous nature of compensatory proliferation. However, we cannot rule out the possibility that there are additional mechanisms that could suppress cell division of neighboring cells next to the dividing and apoptotic cells. For instance, a paralog of YAP, a transcriptional co-activator with a PDZ-binding motif (TAZ), is shown to be excluded from the nucleus by extrinsic compression and can cause lateral inhibition in cell fate specification.[34] Indeed, the neighboring cells that experienced a negative strain, i.e., compression, did not undergo cell division (Figure 3E). Moreover, it will be interesting to investigate how extracellular-signal-regulated kinase (ERK), which is shown to act as a survival factor for neighboring cells,[35,36] and calcium, which promotes cell extrusion,[37] contributes to compensatory proliferation.

Together, our findings from a mechanical perspective complement the current biochemical understanding of apoptosis-induced compensatory growth and provide additional insights into cellular functions of how tissue precisely maintains homeostasis.

Limitations of the study

Although we showed that the neighboring cells with YAP nuclear translocation are associated with cell division (Figures S2D and S2E), the mechanisms of how YAP nuclear translocation leads to cell-cycle progression in the context of apoptosis-induced

Figure 4. Compensatory proliferation requires force propagation through the substrate

(A–F) Experiments using mini-tissues to reduce force propagation.

(A) MDCK YAP-GFP cells (right) confined to a circular pattern of 100 μm diameter fibronectin (left).

(B) A heatmap with vectors showing the bead displacement at 1 min after laser-induced apoptosis.

(C) Average bead displacement at different distances from the apoptotic cell (row number) at 1 min after apoptosis. Data are mean ± SD, one-way ANOVA, and Levene test followed by a Tukey-Kramer test. n = 5 ROIs in 5 independent experiments.

(D) Time-lapse images of MDCK YAP-GFP monolayer before and 2 h after laser-induced apoptosis.

(E) Evolution of the nuclear/cytosolic (Nuc/Cyt) YAP-GFP ratio in cells surrounding an apoptotic cell. Data are mean ± SD. n = 20 cells in 6 ROIs from 6 independent experiments.

(F) A scatter plot showing how cells without YAP nuclear translocation (blue) correlate with the nuclear area and average bead displacement. Nuclear area and bead displacement were measured at 1 min before and after apoptosis. n = 29 cells in 6 ROIs from 6 independent experiments. Same classifications of YAP translocation are used as in Figure 3D.

(G–N) Experiments with the substrate that strongly adheres to a glass-bottom dish to reduce force propagation. (G) Schematic illustration of the experimental setup with an APTES-coated adhesive glass-bottom dish. (H) A heatmap with vectors showing the bead displacement at 1 min after laser-induced apoptosis. (I) Average bead displacement at different distances from the apoptotic cell (row number) at 1 min after apoptosis. Data are mean ± SD, one-way ANOVA, and Levene test followed by a Tukey-Kramer test. n = 6 ROIs in 6 independent experiments. (J) Time-lapse images showing MDCK YAP-GFP monolayer before and after laser-induced apoptosis (asterisk).

(K) Evolution of YAP-GFP ratio in cells surrounding an apoptotic cell. Data are mean ± SD. n = 23 cells in 4 ROIs from 4 independent experiments.

(L) A scatter plot showing how cells without YAP nuclear translocation (blue) correlate with the nuclear area and bead displacement. Nuclear area and bead displacement were measured at 1 min before and after apoptosis. n = 35 cells in 5 ROIs from 5 independent experiments.

(M) Time-lapse images of MDCK FUCCI cells surrounding a spontaneous apoptotic cell (white arrowhead). The cyan dashed line represents the boundary between row 2 and row 3 from the apoptotic cell.

(N) Probability of cell division within 24 h after spontaneous cell extrusion. Data are from the neighboring cells associated (gray) and not associated (white) with apoptosis on different substrates, i.e., less-adhesive (Figure 1A) and APTES-coated adhesive substrates (Figure 4G). Data are mean ± SD, *$p < 0.05$ and ***$p < 0.001$, Kruskal-Wallis rank-sum test followed by Steel-Dwass test. n = 54 ROIs in 6 independent experiments (each case with uncoated dish), n = 54 ROIs in 4 independent experiments (each case with APTES-coated dish).

(O) A model of apoptosis-induced compensatory proliferation. Scale bars, 20 μm.

proliferation need to be investigated further. Perturbing YAP activity or its nuclear transport would provide insight into this process. However, it is known that inhibiting YAP prevents cell division regardless of apoptosis,[38] making it difficult to definitively assess its role in compensatory proliferation. Additionally, apoptosis-induced proliferation has been observed in a wide range of cancers, including breast cancer, melanoma, and glioma cells.[39–42] It remains to be determined whether the mechanisms identified in this study are general to other contexts, including tumor pathology.

STAR★METHODS

Detailed methods are provided in the online version of this paper and include the following:

- KEY RESOURCES TABLE
- RESOURCE AVAILABILITY
  - Lead contact
  - Materials availability
  - Data and code availability
- EXPERIMENTAL MODEL AND SUBJECT DETAILS
  - Cell lines
- METHOD DETAILS
  - Antibodies
  - Cell culture and drug treatment
  - Microfabrication of silicone gel substrate
  - Substrate–glass adhesion
  - Microcontact printing
  - Laser induction of apoptosis
  - Traction force microscopy (TFM)
  - Laser ablation
  - Immunocytochemistry
  - Microscopy imaging
- QUANTIFICATION AND STATISTICAL ANALYSIS
  - Analysis of cell-cycle progression and cell division
  - Measurement of bead displacement
  - Quantification of cellular deformation (strain)
  - Recoil velocity
  - Measurement of YAP-GFP fluorescence intensity
  - Nuclear size and nuclear pore
  - Statistical analysis

SUPPLEMENTAL INFORMATION

Supplemental information can be found online at https://doi.org/10.1016/j.devcel.2023.01.005.

ACKNOWLEDGMENTS

This work is supported by the Singapore Ministry of Education Tier2 grant (MOE2015-T2-1-116 and T2EP30220-0033 to Y.T.), the USPC-NUS collaborative program (to Y.T and B.L.), the European Research Council (ERC-2020-ADG-101019835 to B.L.), LABEX Who Am I? (ANR-11-LABX-0071 to B.L.), the Ligue Contre le Cancer (Equipe labellisée 2019), the Agence Nationale de la Recherche ("Myofuse" ANR-19-CE13-0016 to B.L.), the CNRS through 80|Prime program (to B.L.), the Japan Society for the Promotion of Science Overseas Research Fellowships (to T.K.), and the Mechanobiology Institute Seed fund (J.P., T.H., and Y.T.). We are grateful to Lars Hufnagel for sharing MDCK FUCCI cell lines and Marius Sudol for the YAP1-mGFP plasmids. The authors thank the MBI microscopy core for imaging and Andrew Wong from the MBI science communication core for editing the manuscript.

AUTHOR CONTRIBUTIONS

T.K., I.Y., and Y.T. designed the experiments. T.K., I.Y., Y.P., A.P.L., M.L., and X.T. performed the experiments. T.K., I.Y., Y.L., M.L., and M.S. analyzed the data. Y.L., J.P., T.H., and B.L. contributed quantitative analyses and theoretical interpretation. I.Y. generated cell lines. T.K. and Y.T. wrote the manuscript. Y.T. oversaw the project. All authors discussed the results and commented on the manuscript.

DECLARATION OF INTERESTS

The authors declare no competing interests.

Received: September 20, 2021
Revised: July 9, 2022
Accepted: January 26, 2023
Published: February 16, 2023

REFERENCES

1. Fuchs, Y., and Steller, H. (2011). Programmed cell death in animal development and disease. Cell *147*, 742–758. https://doi.org/10.1016/j.cell.2011.10.033.
2. Haynie, J.L., and Bryant, P.J. (1977). The effects of X-rays on the proliferation dynamics of cells in the imaginal wing disc of Drosophila melanogaster. Wilhelm Roux. Arch. Dev. Biol. *183*, 85–100. https://doi.org/10.1007/BF00848779.
3. Fogarty, C.E., and Bergmann, A. (2015). The Sound of silence: signaling by apoptotic cells. Curr. Top. Dev. Biol. *114*, 241–265. https://doi.org/10.1016/bs.ctdb.2015.07.013.
4. Fuchs, Y., and Steller, H. (2015). Live to die another way: modes of programmed cell death and the signals emanating from dying cells. Nat. Rev. Mol. Cell Biol. *16*, 329–344. https://doi.org/10.1038/nrm3999.
5. Fan, Y., and Bergmann, A. (2008). Distinct mechanisms of apoptosis-induced compensatory proliferation in proliferating and differentiating tissues in the Drosophila eye. Dev. Cell *14*, 399–410. https://doi.org/10.1016/j.devcel.2008.01.003.
6. Morata, G., Shlevkov, E., and Pérez-Garijo, A. (2011). Mitogenic signaling from apoptotic cells in Drosophila. Dev. Growth Differ. *53*, 168–176. https://doi.org/10.1111/j.1440-169X.2010.01225.x.
7. Pérez-Garijo, A., Martín, F.A., and Morata, G. (2004). Caspase inhibition during apoptosis causes abnormal signalling and developmental aberrations in Drosophila. Development *131*, 5591–5598. https://doi.org/10.1242/dev.01432.
8. Ryoo, H.D., Gorenc, T., and Steller, H. (2004). Apoptotic cells can induce compensatory cell proliferation through the JNK and the Wingless signaling pathways. Dev. Cell *7*, 491–501. https://doi.org/10.1016/j.devcel.2004.08.019.
9. Smith-Bolton, R.K., Worley, M.I., Kanda, H., and Hariharan, I.K. (2009). Regenerative growth in Drosophila imaginal discs is regulated by Wingless and Myc. Dev. Cell *16*, 797–809. https://doi.org/10.1016/j.devcel.2009.04.015.
10. Castellone, M.D., Teramoto, H., Williams, B.O., Druey, K.M., and Gutkind, J.S. (2005). Prostaglandin E2 promotes colon cancer cell growth through a Gs-axin-beta-catenin signaling axis. Science *310*, 1504–1510. https://doi.org/10.1126/science.1116221.
11. Li, F., Huang, Q., Chen, J., Peng, Y., Roop, D.R., Bedford, J.S., and Li, C.Y. (2010). Apoptotic cells activate the "phoenix rising" pathway to promote wound healing and tissue regeneration. Sci. Signal. *3*, ra13. https://doi.org/10.1126/scisignal.2000634.
12. Rosenblatt, J., Raff, M.C., and Cramer, L.P. (2001). An epithelial cell destined for apoptosis signals its neighbors to extrude it by an

actin- and myosin-dependent mechanism. Curr. Biol. *11*, 1847–1857. https://doi.org/10.1016/s0960-9822(01)00587-5.

13. Teng, X., Qin, L., Le Borgne, R., and Toyama, Y. (2017). Remodeling of adhesion and modulation of mechanical tensile forces during apoptosis in Drosophila epithelium. Development *144*, 95–105. https://doi.org/10.1242/dev.139865.

14. Kocgozlu, L., Saw, T.B., Le, A.P., Yow, I., Shagirov, M., Wong, E., Mège, R.M., Lim, C.T., Toyama, Y., and Ladoux, B. (2016). Epithelial cell packing induces distinct modes of cell extrusions. Curr. Biol. *26*, 2942–2950. https://doi.org/10.1016/j.cub.2016.08.057.

15. Michael, M., Meiring, J.C.M., Acharya, B.R., Matthews, D.R., Verma, S., Han, S.P., Hill, M.M., Parton, R.G., Gomez, G.A., and Yap, A.S. (2016). Coronin 1B reorganizes the architecture of F-actin networks for contractility at steady-state and apoptotic adherens junctions. Dev. Cell *37*, 58–71. https://doi.org/10.1016/j.devcel.2016.03.008.

16. Le, A.P., Rupprecht, J.F., Mège, R.M., Toyama, Y., Lim, C.T., and Ladoux, B. (2021). Adhesion-mediated heterogeneous actin organization governs apoptotic cell extrusion. Nat. Commun. *12*, 397. https://doi.org/10.1038/s41467-020-20563-9.

17. Toyama, Y., Peralta, X.G., Wells, A.R., Kiehart, D.P., and Edwards, G.S. (2008). Apoptotic force and tissue dynamics during Drosophila embryogenesis. Science *321*, 1683–1686. https://doi.org/10.1126/science.1157052.

18. Monier, B., Gettings, M., Gay, G., Mangeat, T., Schott, S., Guarner, A., and Suzanne, M. (2015). Apico-basal forces exerted by apoptotic cells drive epithelium folding. Nature *518*, 245–248. https://doi.org/10.1038/nature14152.

19. Teo, J.L., Tomatis, V.M., Coburn, L., Lagendijk, A.K., Schouwenaar, I.M., Budnar, S., Hall, T.E., Verma, S., McLachlan, R.W., Hogan, B.M., et al. (2020). Src kinases relax adherens junctions between the neighbors of apoptotic cells to permit apical extrusion. Mol. Biol. Cell *31*, 2557–2569. https://doi.org/10.1091/mbc.E20-01-0084.

20. Teng, X., and Toyama, Y. (2011). Apoptotic force: active mechanical function of cell death during morphogenesis. Dev. Growth Differ. *53*, 269–276. https://doi.org/10.1111/j.1440-169X.2011.01251.x.

21. Saw, T.B., Doostmohammadi, A., Nier, V., Kocgozlu, L., Thampi, S., Toyama, Y., Marcq, P., Lim, C.T., Yeomans, J.M., and Ladoux, B. (2017). Topological defects in epithelia govern cell death and extrusion. Nature *544*, 212–216. https://doi.org/10.1038/nature21718.

22. Discher, D.E., Janmey, P., and Wang, Y.L. (2005). Tissue cells feel and respond to the stiffness of their substrate. Science *310*, 1139–1143. https://doi.org/10.1126/science.1116995.

23. Thomas, M., Ladoux, B., and Toyama, Y. (2020). Desmosomal junctions govern tissue integrity and actomyosin contractility in apoptotic cell extrusion. Curr. Biol. *30*, 682–690.e5. https://doi.org/10.1016/j.cub.2020.01.002.

24. Hara, Y., Shagirov, M., and Toyama, Y. (2016). Cell boundary elongation by non-autonomous contractility in cell oscillation. Curr. Biol. *26*, 2388–2396. https://doi.org/10.1016/j.cub.2016.07.003.

25. Lou, Y., Kawaue, T., Yow, I., Toyama, Y., Prost, J., and Hiraiwa, T. (2022). Interfacial friction and substrate deformation mediate long-range signal propagation in tissues. Biomech. Model. Mechanobiol. *21*, 1511–1530. https://doi.org/10.1007/s10237-022-01603-3.

26. Sudol, M. (2013). YAP1 oncogene and its eight isoforms. Oncogene *32*, 3922. https://doi.org/10.1038/onc.2012.520.

27. Dupont, S., Morsut, L., Aragona, M., Enzo, E., Giulitti, S., Cordenonsi, M., Zanconato, F., Le Digabel, J., Forcato, M., Bicciato, S., et al. (2011). Role of YAP/TAZ in mechanotransduction. Nature *474*, 179–183. https://doi.org/10.1038/nature10137.

28. Dong, J., Feldmann, G., Huang, J., Wu, S., Zhang, N., Comerford, S.A., Gayyed, M.F., Anders, R.A., Maitra, A., and Pan, D. (2007). Elucidation of a universal size-control mechanism in Drosophila and mammals. Cell *130*, 1120–1133. https://doi.org/10.1016/j.cell.2007.07.019.

29. Sakaue-Sawano, A., Kurokawa, H., Morimura, T., Hanyu, A., Hama, H., Osawa, H., Kashiwagi, S., Fukami, K., Miyata, T., Miyoshi, H., et al. (2008). Visualizing spatiotemporal dynamics of multicellular cell-cycle progression. Cell *132*, 487–498. https://doi.org/10.1016/j.cell.2007.12.033.

30. Elosegui-Artola, A., Andreu, I., Beedle, A.E.M., Lezamiz, A., Uroz, M., Kosmalska, A.J., Oria, R., Kechagia, J.Z., Rico-Lastres, P., Le Roux, A.L., et al. (2017). Force triggers YAP nuclear entry by regulating transport across nuclear pores. Cell *171*, 1397–1410.e14. https://doi.org/10.1016/j.cell.2017.10.008.

31. Trepat, X., Wasserman, M.R., Angelini, T.E., Millet, E., Weitz, D.A., Butler, J.P., and Fredberg, J.J. (2009). Physical forces during collective cell migration. Nature Phys. *5*, 426–430. https://doi.org/10.1038/nphys1269.

32. Mesa, K.R., Kawaguchi, K., Cockburn, K., Gonzalez, D., Boucher, J., Xin, T., Klein, A.M., and Greco, V. (2018). Homeostatic epidermal stem cell self-renewal is driven by local differentiation. Cell Stem Cell *23*, 677–686.e4. https://doi.org/10.1016/j.stem.2018.09.005.

33. Lherbette, M., Dos Santos, Á., Hari-Gupta, Y., Fili, N., Toseland, C.P., and Schaap, I.A.T. (2017). Atomic Force Microscopy micro-rheology reveals large structural inhomogeneities in single cell-nuclei. Sci. Rep. *7*, 8116. https://doi.org/10.1038/s41598-017-08517-6.

34. Xia, P., Gütl, D., Zheden, V., and Heisenberg, C.P. (2019). Lateral inhibition in cell specification mediated by mechanical signals modulating TAZ activity. Cell *176*, 1379–1392.e14. https://doi.org/10.1016/j.cell.2019.01.019.

35. Gagliardi, P.A., Dobrzyński, M., Jacques, M.A., Dessauges, C., Ender, P., Blum, Y., Hughes, R.M., Cohen, A.R., and Pertz, O. (2021). Collective ERK/Akt activity waves orchestrate epithelial homeostasis by driving apoptosis-induced survival. Dev. Cell *56*, 1712–1726.e6. https://doi.org/10.1016/j.devcel.2021.05.007.

36. Valon, L., Davidović, A., Levillayer, F., Villars, A., Chouly, M., Cerqueira-Campos, F., and Levayer, R. (2021). Robustness of epithelial sealing is an emerging property of local ERK feedback driven by cell elimination. Dev. Cell *56*, 1700–1711.e8. https://doi.org/10.1016/j.devcel.2021.05.006.

37. Takeuchi, Y., Narumi, R., Akiyama, R., Vitiello, E., Shirai, T., Tanimura, N., Kuromiya, K., Ishikawa, S., Kajita, M., Tada, M., et al. (2020). Calcium wave promotes cell extrusion. Curr. Biol. *30*, 670–681.e6. https://doi.org/10.1016/j.cub.2019.11.089.

38. Cebola, I., Rodríguez-Seguí, S.A., Cho, C.H.-H., Bessa, J., Rovira, M., Luengo, M., Chhatriwala, M., Berry, A., Ponsa-Cobas, J., Maestro, M.A., et al. (2015). TEAD and YAP regulate the enhancer network of human embryonic pancreatic progenitors. Nat. Cell Biol. *17*, 615–626. https://doi.org/10.1038/ncb3160.

39. Donato, A.L., Huang, Q., Liu, X., Li, F., Zimmerman, M.A., and Li, C.Y. (2014). Caspase 3 promotes surviving melanoma tumor cell growth after cytotoxic therapy. J. Invest. Dermatol. *134*, 1686–1692. https://doi.org/10.1038/jid.2014.18.

40. Kurtova, A.V., Xiao, J., Mo, Q., Pazhanisamy, S., Krasnow, R., Lerner, S.P., Chen, F., Roh, T.T., Lay, E., Ho, P.L., et al. (2015). Blocking PGE2-induced tumour repopulation abrogates bladder cancer chemoresistance. Nature *517*, 209–213. https://doi.org/10.1038/nature14034.

41. Mao, P., Smith, L., Xie, W., and Wang, M. (2013). Dying endothelial cells stimulate proliferation of malignant glioma cells via a caspase 3-mediated pathway. Oncol. Lett. *5*, 1615–1620. https://doi.org/10.3892/ol.2013.1223.

42. Ryoo, H.D., and Bergmann, A. (2012). The role of apoptosis-induced proliferation for regeneration and cancer. Cold Spring Harb. Perspect. Biol. *4*, a008797. https://doi.org/10.1101/cshperspect.a008797.

43. Schindelin, J., Arganda-Carreras, I., Frise, E., Kaynig, V., Longair, M., Pietzsch, T., Preibisch, S., Rueden, C., Saalfeld, S., Schmid, B., et al. (2012). Fiji: an open-source platform for biological-image analysis. Nat. Methods *9*, 676–682. https://doi.org/10.1038/nmeth.2019.

44. Tinevez, J.Y., Perry, N., Schindelin, J., Hoopes, G.M., Reynolds, G.D., Laplantine, E., Bednarek, S.Y., Shorte, S.L., and Eliceiri, K.W. (2017).

TrackMate: an open and extensible platform for single-particle tracking. Methods *115*, 80–90. https://doi.org/10.1016/j.ymeth.2016.09.016.

45. Meijering, E., Dzyubachyk, O., and Smal, I. (2012). Methods for cell and particle tracking. Methods Enzymol. *504*, 183–200. https://doi.org/10.1016/B978-0-12-391857-4.00009-4.
46. Carpenter, A.E., Jones, T.R., Lamprecht, M.R., Clarke, C., Kang, I.H., Friman, O., Guertin, D.A., Chang, J.H., Lindquist, R.A., Moffat, J., et al. (2006). CellProfiler: image analysis software for identifying and quantifying cell phenotypes. Genome Biol. *7*, R100. https://doi.org/10.1186/gb-2006-7-10-r100.
47. Thielicke, W., and Stamhuis, E.J. (2014). PIVlab – towards user-friendly, affordable and accurate digital particle image velocimetry in MATLAB. J. Open Res. Softw. *2*, e30. https://doi.org/10.5334/jors.bl.
48. Vedula, S.R.K., Hirata, H., Nai, M.H., Brugués, A., Toyama, Y., Trepat, X., Lim, C.T., and Ladoux, B. (2014). Epithelial bridges maintain tissue integrity during collective cell migration. Nat. Mater. *13*, 87–96. https://doi.org/10.1038/ncomms7111.
49. Davis, L.I., and Blobel, G. (1986). Identification and characterization of a nuclear pore complex protein. Cell *45*, 699–709. https://doi.org/10.1016/0092-8674(86)90784-1.

STAR★METHODS

KEY RESOURCES TABLE

REAGENT or RESOURCE	SOURCE	IDENTIFIER
Antibodies		
Mouse Anti-mAb414 antibody	BioLegend	CAT# 902907; RRID: AB_2734672
Mouse Anti-YAP antibody	Novus biologicals	CAT# H00010413-M01; RRID: AB_549187
Chicken Anti-GFP antibody	Aves Labs	CAT# GFP-1020; RRID: AB_10000240
Goat Alexa Fluor 488 anti-mouse IgG (H+L) antibody	Invitrogen	CAT# A-11001; RRID: AB_2534069
Goat Alexa Fluor 568 anti-mouse IgG (H+L) antibody	Invitrogen	CAT# A-11004; RRID: AB_2534072
Goat Alexa Fluor 488 anti-Chicken IgY (H+L) antibody	Invitrogen	CAT# A-11039; RRID: AB_2534096
Chemicals, peptides, and recombinant proteins		
TurboFectin 8.0	OriGene Technologies	CAT# TF81005
Puromycin	Gibco	CAT# A1113803
Penicillin-Streptomycin	Gibco	CAT# 15140
Fibronectin	Gibco	CAT# 33016015
NSC23766 Trihydrochloride	Sigma-Aldrich	CAT# SML0952
CY52-276A	Dow Corning	CAT# 2624028
CY52-276B	Dow Corning	CAT# 2624052
3-aminopropyl trimethoxysilane (APTES)	Sigma-Aldrich	CAT# 440140
Polydimethylsiloxane, PDMS	Dow Corning	Sylgard 184
Hoechst 33342	Invitrogen	CAT# H3570
Carboxylated red fluorescent beads	Molecular Probes	CAT# F8801
Carboxylated dark-red fluorescent beads	Molecular Probes	CAT# F8807
Experimental models: Cell lines		
Dog: MDCK	James W. Nelson lab, Stanford University	RRDI: CVCL_0422
Dog: MDCK E-cadherin-GFP	James W. Nelson lab, Stanford University	N/A
Dog: MDCK FUCCI	Lars Hufnagel lab, European Molecular Biology Laboratory	N/A
Dog: MDCK YAP-GFP	This study	N/A
Dog: MDCK Paxillin-GFP	This study	N/A
Recombinant DNA		
cDNA YAP1	OriGene Technologies	NM_001195044
pLenti-C-mGFP-P2A-Puro	OriGene Technologies	CAT# PS100093
pLenti-C-YAP1-mGFP-P2A-Puro	This study	N/A
cDNA Paxillin	OriGene Technologies	NM_002859
pLenti-C-Paxillin-mGFP-P2A-Puro	This study	N/A
Software and algorithms		
Fiji	Schindelin et al.[43]	RRID:SCR_002285
TrackMate, Fiji plug-in	Tinevez et al.[44]	https://imagej.net/imagej-wiki-static/TrackMate
MtrackJ, Fiji plug-in	Meijering et al.[45]	https://imagescience.org/meijering/software/mtrackj/
StarDist, Fiji plug-in	Carpenter et al.[46]	https://imagej.net/plugins/stardist
R	R-project	RRID: SCR_001905
Rstudio	Rstudio	RRID: SCR_000432
MATLAB	MathWorks	RRID: SCR_001622

(*Continued on next page*)

Continued

REAGENT or RESOURCE	SOURCE	IDENTIFIER
PIVlab, MATLAB code	[47]	https://jp.mathworks.com/matlabcentral/fileexchange/27659-pivlab-particle-image-velocimetry-piv-tool-with-gui
Recoil velocity, customized MATLAB code	Hara et al.[24]	Yusuke Toyama Lab
Other		
Nikon BioStation IM-Q	Nikon	BioStation IM-Q
NikonA1R MP laser scanning confocal microscope	Nikon	Nikon A1R
Nikon Eclipse Ti-E Inverted microscope	Nikon	Nikon Eclipse Ti-E

RESOURCE AVAILABILITY

Lead contact

Further information and requests for resources should be directed to and will be fulfilled by the Lead Contact, Yusuke Toyama (dbsty@nus.edu.sg).

Materials availability

Cell lines generated for this study are available on request to the corresponding authors. This study did not generate new unique reagents.

Data and code availability

- All data reported in this paper will be shared by the lead contact upon request.
- This paper does not report original code.
- Any additional information required to reanalyze the data reported in this paper is available from the lead contact upon request.

EXPERIMENTAL MODEL AND SUBJECT DETAILS

Cell lines

Madin-Darby canine kidney strain II wild type (MDCK WT, *Canis familiaris*, female) and MDCK E-cadherin-GFP were kindly provided by James W. Nelson (Stanford University). The MDCK FUCCI stable cell line was kindly provided by Lars Hufnagel (European Molecular Biology Laboratory). FUCCI, a cell cycle indicator, effectively labels individual nuclei in G1 phase red (mKO2-hCdt1) and those in S/G2/M phase green (mAG-hGeminin).[29] Yes-associated protein (YAP) is known to respond to mechanical signals and act as a growth-promoting cofactor.[26,30] To monitor YAP localization in cells, we constructed MDCK YAP-GFP cells which stably expressing a YAP1-mGFP fusion protein. cDNA encoding YAP1 (NM_001195044) was cloned into a third-generation lentiviral plasmid, pLenti-C-mGFP-P2A-Puro (OriGene Technologies). To produce lentivirus encoding for YAP1-mGFP, HEK293T cells were transfected with pLenti-C-YAP1-mGFP-P2A-Puro using TurboFectin 8.0 (OriGene Technologies). Viral particles were concentrated, and lentiviral transduction was performed on MDCK WT cells using lentiviral packaging plasmids (OriGene Technologies). MDCK YAP-GFP cell clones were selected with puromycin (Gibco) and then sorted by FACS. To monitor focal adhesion, we constructed MDCK paxillin-GFP cells using paxillin (NM_002859) human-tagged ORF clone lentiviral particles (pLenti-C-Paxillin-mGFP-P2A-Puro) with the same procedure as the construction of MDCK YAP-GFP cells. The distribution of YAP-GFP signal was similar to that of endogenous YAP (Figure S2A).

METHOD DETAILS

Antibodies

The following primary and secondary antibodies were used for immunocytochemistry: mouse mAb414 antibody (1:1000, BioLegend); mouse anti-YAP antibody (1:250, Novus biologicals, Littleton, CO); chicken anti-GFP antibody (1:1000, Aves Labs); goat Alexa Fluor 488 anti-mouse IgG (H+L) antibody (1:1000, Invitrogen); goat Alexa Fluor 568 anti-mouse IgG (H+L) antibody (1:1000, Invitrogen); and Goat Alexa Fluor 488 anti-chicken IgY (H+L) antibody (1:1000, Invitrogen).

Cell culture and drug treatment

MDCK cell lines were maintained in Dulbecco's modified eagle medium (DMEM, Gibco) supplemented with 10% fetal bovine serum (FBS, Gibco), and 100 units/ml penicillin-streptomycin (Gibco), and kept in a 37°C humidified incubator containing 5% CO_2. Cells (1-2 x 10^5) were seeded onto a silicone gel substrate coated with pure fibronectin (20 μg/ml, Gibco). To arrest the cell cycle

and synchronize cells at G0/G1 phase, cells were serum-starved for 24 h. Before microscopic imaging, serum-free media was replaced with fresh DMEM containing 10% FBS. To inhibit Rac1, MDCK monolayers were treated with NSC-23766 (200 μM, Sigma-Aldrich) in culture media for 30 min prior to imaging.

Microfabrication of silicone gel substrate

Soft Polydimethylsiloxane (PDMS) gel was used as the substrate in all experiments. To prepare the substrate with a stiffness of 10–20 kPa Young's modulus, CY52-276A and CY52-276B components (Dow Corning) were mixed at 1:1 (wt/wt) ratio. The mixed gel was spin-coated onto the glass-bottom Petri dishes (IWAKI) at 1000 rpm for 1 min and then cured at 80 °C for 2 h. The flat gel thickness was 50μm (Figure 1A).

Substrate–glass adhesion

For weaker adhesion between the silicone gel substrate and glass-bottom Petri dish (IWAKI), soft silicone elastomer substrate (CY52-276A/B mixture, 1:1 [wt/wt]) was spin-coated (1000 rpm, 1 min) on a dish without a plasma treatment, which is a procedure for traction force microscopy. For stronger adhesion, 3-aminopropyl trimethoxysilane (APTES) was used as a chemical crosslinking agent was used (Figure 4G). The dish was silanized with 5% APTES (Sigma-Aldrich) in ethanol for 30 min, rinsed with ethanol, and cured at 80 °C for 60 min. The soft silicone elastomer substrate (CY52-276A/B blended, 1:1 [wt/wt]) was then spin-coated (1000 rpm, 1 min) onto an APTES-coated dish.

Microcontact printing

To confine the cells within a circular pattern (100 μmΦ) on the substrate, we used a micro-contact printing technique.[16] Silicon wafers with circular patterns were fabricated using SU-8 photoresist for soft lithography. To form stamps, PDMS (Sylgard 184, Dow Corning) with a crosslinker to silicone elastomer of 1:10 ratio (wt/wt) ratio was poured onto the wafer, degassed, and then cured at 80°C for 2 h. The stamps were coated with a mixture of 50 μg/mL pure fibronectin (Roche) and 25 μg/mL Cy5-conjugated fibronectin (Cy5-FN, GE Healthcare) for 1 h. The pattern of interest was first stamped onto a Polyvinyl Alcohol membrane prepared from 5% PVA solution (Sigma), and the membrane was inverted onto the soft gel substrate (CY52-276A/B mixture, 1:1 [wt/wt]). The membrane was dissolved, and the non-patterned areas were passivated by incubation with 2% Pluronics for 2 h. Finally, cells were seeded onto the substrate as described above. Circularly patterned mini-tissues were synchronized at G0/G1 phase and imaged using a NikonA1R MP laser scanning confocal microscope.

Laser induction of apoptosis

Laser-based apoptosis induction was performed using NikonA1R MP laser scanning confocal microscope with a Nikon Apo 60x/1.40 oil-immersion objective.[14] To induce DNA damage for a single cell, a UV laser (355 nm, 300 ps pulse duration, 1 kHz repetition rate, PowerChip PNV-0150-100, team photonics) with a laser power of 25-50 nW at the back aperture of the objective was focused on the nucleus for 3-5 s.[23] The onset of apoptotic extrusion, defined by cell shrinkage and nuclear condensation, was observed within 5-10 min following laser irradiation.[16] The nucleus was stained with Hoechst 33342 (1 μg/ml, Invitrogen) in culture medium for 1 h and washed before the laser induction experiment.

Traction force microscopy (TFM)

Traction force microscopy is a non-invasive technique that measures the local substrate deformations by imaging the displacements of fluorescent beads on the surface of soft elastic gel.[48] The substrate spin-coated Petri dish was silanized with 5% APTES in ethanol for 15 min, rinsed with ethanol, and cured at 80 °C for 60 min. Carboxylated red or dark-red fluorescent beads (Molecular Probes) were functionalized on the substrate at a 1:500 dilution in distilled water for 10 min. The beads were then passivated with Tris (100mM, Sigma) for 30 min and washed with distilled water. Pure fibronectin (20 μg/ml) was incubated on the substrate at 37 °C for 1 h prior to cell seeding. Cells and beads were imaged using a NikonA1R MP laser scanning confocal microscope or Nikon BioStation IM-Q. Images were taken every 1 or 5 min with z step = 0.75 μm.

Laser ablation

For junctional ablation, we used MDCK E-cadherin-GFP cells seeded on the silicone gel substrate overlaid on the glass bottom dish. The laser ablation experiment was performed on a NikonA1R MP laser scanning confocal microscope with Nikon Apo 60x/1.40 oil-immersion objective.[16,24] A UV-laser (355 nm, 300 ps pulse duration, 1 kHz repetition rate, PowerChip PNV-0150-100, team photonics) was focused on the cell-cell junction of the target cell for 0.1 sec at a laser power of 200 nW at the back aperture of the objective (Figure S1A). Time-lapse image series were started 10 sec before the ablation and acquired every 1 sec.

Immunocytochemistry

MDCK cells were fixed with 4% paraformaldehyde for 10 min at room temperature, permeabilized and blocked with 0.1% Triton X-100 in 3% BSA/PBS for 30 min. The nuclear pore complex (NPC) was stained with the monoclonal antibody mAb414 (1:1000, BioLegend) which is widely used to detect functionally mature NPCs.[49] MDCK YAP-GFP cells were treated with anti-YAP (H00010413-M01, 1:250, Novus biologicals, Littleton, CO) and anti-GFP antibodies (GFP-1020, 1:1000, Aves Labs). Cells were washed with PBS and incubated with secondary antibodies containing 0.1% Triton X-100 in 3% BSA/PBS for 1 h at room

temperature. The nucleus was labeled with Hoechst 33342 (1 μg/ml). Confocal images were acquired using a W1 spinning disk confocal microscope.

Microscopy imaging

Prior to imaging, all MDCK monolayer tissues were synchronized at G0/G1 phase, and then fresh media containing serum was added. Cell density was kept at 60-70 cells per 100 x 100 μm^2 for imaging. Phase-contrast and fluorescence time-lapse imaging for the MDCK FUCCI monolayer was performed on a Nikon BioStation IM-Q with a 20x objective. For confocal time-lapse imaging and TFM, the nucleus was labeled with Hoechst 33342 prior to imaging, and then images were acquired using a NikonA1R MP laser scanning confocal microscope with a Nikon Apo 60x/1.40 oil-immersion objective under the control of NIS-Elements with a 0.75-μm interval-z scanning setting. Confocal fluorescence imaging for fixed MDCK monolayer tissues was performed using a Nikon Eclipse Ti-E inverted microscope equipped with a W1 spinning disk and a 100x/1.45 oil-immersion objective under the control of MetaMorph with a 0.5-μm interval-z scanning setting.

QUANTIFICATION AND STATISTICAL ANALYSIS

Analysis of cell-cycle progression and cell division

To analyze the history of cells around an apoptotic cell within the MDCK-FUCCI monolayer, we recorded apoptotic events and individual cell-cycle progression and cell divisions within the region of interest (ROI, 160 x 160 μm) containing a single extruding cell in the center. For control, ROIs without extruding cells were randomly selected from images that were used for selecting ROIs with apoptosis (Figure 2F). To quantify the cell-cycle progression of MDCK FUCCI cells, we performed automatic cell tracking and measurement of mKO1 and mAG fluorescence intensities using a Fiji plug-in TrackMate,[44] and obtained individual mean fluorescence intensity profiles. The timings of cell-cycle phase transition (G1-S, S-G2, and G2-M phase) were automatically calculated from the fluorescence intensity profiles using an R package 'segmented'. Briefly, mKO1 and mAG fluorescence intensity were plotted against time and then fitted to the piecewise regression models. Breakpoints where the regression lines intersected in each fluorescence were defined as the transition time points. The first and second breakpoints in mAG were defined as G1-S and G2-M phase transitions, respectively. The second breakpoint in mKO1 was defined as S-G2 phase transition. To calculate the probability of cell division in each row, the number of cell divisions was divided by the total number of cells in each row.

Measurement of bead displacement

Bead displacement in the TFM experiment was calculated by particle image velocimetry (PIV) analysis using an open-source MATLAB code PIVlab.[47] The setting, three passes (64x64, 32x32, and 16x16 pixel size interrogation window with 50% overlap each), was used. The radial displacement of the beads was calculated using a custom MATLAB code (Figures 1C–1F). To create kymographs for the average radial velocity of beads, the radial displacement of beads was averaged at each radius (0 to 73 μm, every 1.66 μm) from the center of the apoptotic cell.[14] The extent of mechanical propagation is estimated by the static region, which is the boundary between the radial outward and inward displacements of the beads. The average distance between the static region and the center of the apoptotic cell was calculated from the data set prepared to calculate the average radial velocity of beads, and then we plotted it every 5 min in Figure 1G. The average bead displacement for each cell was calculated from 25 measurement points (5x5) within a ROI (13.12x13.12 μm) with a nuclear centroid nearly in the center (note that the nuclear diameter was estimated to be 10.73±1.452 μm [mean ± s.d.], n = 6719 cells).

Quantification of cellular deformation (strain)

To evaluate the deformation of cells surrounding an apoptotic cell, we calculated cell strain (ε) by dividing the change in cell length (L_t - L_{t0}) by the initial length (L_{T0}). To measure the cell length, we manually traced the outline of the apoptotic and the target cells from the phase images, and then the centroid of the cell was determined using the 'Analyze Particles...' function in Fiji. Finally, the cell length of the target cell was measured along a line connecting their centroids.

Recoil velocity

In order to evaluate the tissue pre-tension, we calculated the recoil velocity after laser ablation at the cell-cell junction. The coordinates (i.e., the axes (x, y)) of two junctional nodes were tracked using the Fiji plug-in MTrackJ[48] (Fig. S1A). The recoil velocity was then calculated as the derivative of the double exponential function using a custom MATLAB code[24].

Measurement of YAP-GFP fluorescence intensity

To quantify the distribution of YAP in cells surrounding an apoptotic cell, we used MDCK YAP-GFP cells and measured nuclear and cytoplasmic YAP-GFP fluorescence intensity. Single nuclei labeled with Hoechst 33342 were automatically segmented using the Fiji plug-in StarDist[49]. Nuclear YAP-GFP fluorescence intensity (I_{nuc}) was measured within the segmented area on a single z-frame where the nuclear centroid was present. The same z-frame was used for manual measurement of cytoplasmic YAP-GFP (I_{cyto}) and background fluorescence intensities (I_{back}). The ratio of nuclear/cytoplasmic YAP-GFP fluorescence intensity ($I_{nuc/cyt}$) in individual cells was calculated as $I_{nuc/cyt} = (I_{nuc} - I_{back}) / (I_{cyt} - I_{back})$. Cells surrounding the apoptotic cell 2 h after laser induction were classified as having "YAP translocation" ($I_{nuc/cyt} \geq 0.5$) or "no YAP translocation" ($I_{nuc/cyt} < 0.5$) status.

Nuclear size and nuclear pore

To quantify the nuclear size, the cross-sectional nuclear area of living cells labeled with FUCCI or a nuclear marker was automatically measured using the Fiji plug-in StarDist. The area measurement was performed on a single z-frame where the nuclear centroid was present. Nuclear volume was estimated on z-series (z step = 0.5μm) using a 3D object counter function of Fiji. Assuming that the nucleus represents an almost perfectly round sphere, the nuclear radius and surface area (area of nuclear envelope, A_{NE}) were calculated from the nuclear volume according to the equations: $V = 4/3\pi r^2$ and $S= 4/3\pi r^2$, where V is the nuclear volume, r is the nuclear radius and S is the nuclear surface area (A_{NE}). To count the number of nuclear pores, a fluorescently labeled nucleus was outlined using Fiji, and then the distribution of mAb414-stained nuclear pores was determined using the Find Maxima function in Fiji. Briefly, the randomly selected nucleus was thresholded and outlined individually on each z-series (z step = 0.5μm), nuclear ROIs were created, and nuclear pores within the ROIs were automatically counted.

Statistical analysis

All experimental data were tested for normality of distribution using the Shapiro-Wilk normality test. Differences were analyzed with the following tests using the R packages: Welch's t-test or Mann-Whitney *U*-test for non-parametric comparison of two groups; Dunnett's test or Tukey-Kramer test after ANOVA and Levene tests for parametric multiple comparisons: or Steel-Dwass test after Kruskal-Wallis rank-sum test for non-parametric multiple comparisons.